A practical theoretical model for Ge-like epitaxial diodes: I. The *I–V* characteristics

Matthew A. Mircovich,[1] (iD) John Kouvetakis,[2] (iD) and José Menéndez[1,a] (iD)

AFFILIATIONS

[1]Department of Physics, Arizona State University, Tempe, Arizona 85287-1504, USA
[2]School of Molecular Sciences, Arizona State University, Tempe, Arizona 85287-1604, USA

a)**Author to whom correspondence should be addressed:** jose.menendez@asu.edu

ABSTRACT

A practical quantitative model is presented to account for the *I–V* characteristics of *pin* diodes based on epitaxial Ge-like materials. The model can be used to quantify how the different material properties and recombination mechanisms affect the diode performance. The importance of dislocations, non-passivated defects, and residual intrinsic layer doping in determining the qualitative shape of the *I–V* curves is discussed in detail. Examples are shown covering literature diodes as well as diodes fabricated with the purpose of validating the theoretical effort.

I. INTRODUCTION

Intense efforts have been devoted since the 1990s to develop technologies that enable the growth of low-defect Ge on Si.[1–3] These advances were followed by the growth and characterization of several generations of devices.[4–7] In more recent times, the field has been enriched and expanded by the introduction of GeSn and GeSiSn alloys[8–10] that extend the detection wavelength range and can reach a direct-gap regime.

The basic component of most of the above devices is Ge-on-Si *pn* or *pin* diodes. The optical and electrical characterization of these devices provides important clues about the material quality and the potential of the technology to contribute to the general area of silicon photonics.[7,11–16] Modern Technology Computer-Aided Design (TCAD) tools can simulate these diodes in great detail, but quantitative fits of experimental *I–V* or responsivity curves are rare. Instead, the analysis of the experimental data is usually based on fits with functions that contain empirical parameters (such as ideality factors or collection efficiencies) or fits with analytical expressions derived from the depletion approximation. Activation energy studies from measurements of the temperature dependence of the *I–V* curves are also quite common. This methodology is not ideal because it is very hard to relate empirical parameters to microscopic properties, and because the interpretation of the data is based on assumptions that are difficult to confirm without explicit modeling. On the other hand, the limited use of TCAD tools to fit

experimental data reveals the need for alternatives that allow the user to easily match experimental and theoretical *I–V* curves, even if these alternatives are more limited in scope compared to those included in commercial packages.

In this paper, we present a model for the *I–V* characteristics of Ge-on-Si diodes that is rigorous enough to allow fitting of experimental data but can be implemented using software and hardware resources commonly available to experimentalists for routine analysis and visualization of experimental data. The model relies on a full numerical solution of the standard semiconductor transport equations. The inherent slowness of this approach is mitigated by the fact that the computation of an *I–V* curve lends itself naturally to multithreading, and therefore we can produce enough *I–V* data points very fast. Furthermore, since different material properties affect the experimental data in characteristic ways, the adjustment of the calculated *I–V* curves to experimental data is greatly facilitated. In this first introduction of the model, we restrict ourselves to homostructure Ge-on-Si *pin* diodes. In subsequent publications, we will discuss extensions to GeSn alloys and to general heterostructure diodes. We will also show how the model can be combined with optical codes to generate realistic predictions of diode responsivities.

The numerical solution of the semiconductor equations allows us to assess the validity of simplified approaches. In some cases, such as the use of activation energies to identify recombination–generation

mechanisms, we find that the conclusions can be erroneous if the temperature dependence of the band structure and electrical properties is not properly accounted for. In this respect, the model is useful to identify the fundamental electronic and transport properties that still need further research to feed accurate models of Ge-on-Si diodes. Our model also demonstrates that in Ge-on-Si *pin* diodes any residual doping in the nominally intrinsic layer interacts with trap-assisted tunneling (TAT) mechanisms to affect the voltage dependence of the reverse-bias current. Simulations under these conditions require an accurate knowledge of the electric field in the structure, which cannot be easily obtained from analytical approximations and requires a numerical solution of Poisson's equation.

We show that a relatively simple description of dislocation-related recombination, consisting of a midgap and a shallow Shockley–Read–Hall (SRH) recombination center, is sufficient to reproduce the *I–V* characteristics of Ge-on-Si diodes grown by different methods, including the standard two-step (low temperature/high temperature) approach for Ge on Si,[4] deposition on germanium-on-insulator (GOI) platforms,[14] and low-temperature approaches based on advanced Ge precursors, as practiced by our group.[17]

The remainder of the paper is organized as follows. In Sec. II, we introduce the model and details on the numerical implementation. In Sec. III, we show how the different model parameters have qualitatively different effects on the experimental *I–V* curves, which facilitates fitting of experimental data. In Sec. IV, we present fits to a few selected examples of Ge-on-Si diodes, including literature data and new devices fabricated for the purpose of validating our model. Finally, in Sec. V, we summarize our conclusions. A detailed discussion of our material parameter choices is given in Appendix A.

II. MODEL DESCRIPTION

A. Basic equations

We will consider a one-dimensional model of a *pin* diode for a two-band semiconductor. We place the origin of the coordinate system at the center of the intrinsic layer, which extends from $z = -d/2$ to $z = d/2$. We assume an acceptor density $N_a(z)$ over a length W_p on one side of the intrinsic layer and a donor density $N_d(z)$ over a length W_n on the other side. In most cases, the acceptor and donor concentrations can be approximated as simple box-like distributions with constant values N_a and N_d. The Poisson and current continuity equations for this system are[18]

$$-\frac{d}{dz}\left[\epsilon(z)\frac{dV}{dz}\right] = 4\pi e[p(z) - n(z) + N_d(z) - N_a(z)], \quad (1)$$

$$\frac{1}{e}\frac{\partial j_n(z)}{\partial z} = R(z), \quad (2)$$

$$\frac{1}{e}\frac{\partial j_p(z)}{\partial z} = -R(z), \quad (3)$$

where $n(z)$ and $p(z)$ are the electron and hole carrier densities, $j_n(z)$ and $j_p(z)$ are the electron and hole current densities, $V(z)$ is the electric potential, $\epsilon(z)$ is the dielectric constant, and $R(z)$ is the recombination–generation rate. The current densities are the sum of a drift and a diffusion component,

$$j_n(z) = -ne\mu_n\frac{dV}{dz} + eD_n\frac{\partial n}{\partial z}, \quad (4)$$

$$j_p(z) = -pe\mu_p\frac{dV}{dz} - eD_p\frac{\partial p}{\partial z}, \quad (5)$$

where μ_n and D_n are the electron mobility and diffusivity and μ_p and D_p the hole mobility and diffusivity. These quantities are related by the generalized Einstein relations as in Eq. (15) of Ref. 19.

The recombination–generation rate is assumed to be given by $R = R_{SRH} + R_{bim}$, where R_{SRH} is given by a sum of Shockley–Read–Hall terms,[18,20]

$$R_{SRH} = \sum_t \frac{[n(z)p(z) - n_i^2]}{\tau_{pt}[n_t + n(z)] + \tau_{nt}[p_t + p(z)]}$$
$$= [n(z)p(z) - n_i^2]r_{SRH}(z). \quad (6)$$

Here, τ_{nt} and τ_{pt} are the electron- and hole-recombination lifetime parameters for trap t, n_i is the intrinsic carrier concentration, and the quantities n_t and p_t are defined as[18]

$$n_t = N_c(T)\exp\left(\frac{E_t - E_c}{k_B T}\right) \quad (7)$$

and

$$p_t = P_v(T)\exp\left(\frac{E_v - E_t}{k_B T}\right), \quad (8)$$

where $N_c(T)$ and $P_v(T)$ are the thermal densities of electrons and holes, respectively, E_c is the conduction band edge, E_v is the valence band edge, and E_t is the trap level energy. From these definitions n_t and p_t can be viewed as the electron and hole concentrations in the conduction and valence bands if the quasi-Fermi levels were at the same energy as the trap level ϵ_t. According to Eqs. (6)–(8), the set of three parameters (τ_{nt}, τ_{pt}, ϵ_t) completely defines the contribution from each trap level to the recombination–generation current. As we will see below, the position of the trap level relative to the band edges has a strong influence not only on the magnitude of this current but also on the overall *I–V* line shapes.

The bimolecular radiative recombination rate is[20]

$$R_{bim}(z) = B_{bim}[n(z)p(z) - n_i^2], \quad (9)$$

where B_{bim} is the bimolecular recombination coefficient. It is also quite straightforward to include Auger recombination and band to band tunneling (BTBT),[20] but we find these are not nearly as important as SRH recombination.

Our primary goal is to solve for the total current density $j = j_n(z) + j_p(z)$. Generalizations of Eqs. (1)–(5) to higher dimensions are straightforward, but the computational cost would make it extremely difficult to attempt any fit of the *I–V* characteristics. This is particularly so the case in the forward-bias regime, for which serial resistance effects require the solution of the semiconductor

06 April 2024 06:05:22

equations not once but multiple times in order to numerically solve the non-linear equation involving the current in a diode with a resistor in series.

From Eqs. (1)–(5), it is apparent that the problem involves three independent functions $\{n(z), p(z), V(z)\}$. For the numerical solution, it is convenient to shift and normalize the potential as

$$v(z) = \frac{eV(z) + F - F_i}{k_B T}, \tag{10}$$

where F is the equilibrium Fermi level, F_i is the intrinsic Fermi level, k_B is the Boltzmann constant, and T is the temperature. We can then write the carrier concentrations as

$$n(z) = n_i u_n(z) \exp[v(z)],$$
$$p(z) = n_i u_p(z) \exp[-v(z)], \tag{11}$$

where n_i is the intrinsic carrier concentration. With these definitions, Eqs. (4) and (5) become, using Einstein's relations,

$$j_n(z) = e D_n n_i \exp[v(z)] \frac{d u_n(z)}{dz}, \tag{12}$$

$$j_p(z) = -e D_p n_i \exp[-v(z)] \frac{d u_p(z)}{dz}. \tag{13}$$

The function set $\{u_n(z), u_p(z), v(z)\}$ are the so-called Slotboom variables and turn out to be convenient for numerical work (Ref. 21). Their physical meaning becomes apparent if we write

$$u_n(z) = \exp\left[\frac{F_n(z) - F}{k_B T}\right],$$
$$u_p(z) = \exp\left[-\frac{F_p(z) - F}{k_B T}\right]. \tag{14}$$

Then, by comparing with the standard quasi-equilibrium analytical expressions for $n(z)$ and $p(z)$, it is easy to see that $F_n(z)$ and $F_p(z)$ can be identified with the electron and hole quasi-Fermi levels.

Equation (1)–(3) can be written in terms of $\{u_n(z), u_p(z), v(z)\}$ as

$$-\frac{d}{dz}\left[\epsilon(z)\frac{dv}{dz}\right] = \frac{4\pi e^2 n_i}{k_B T}\left[u_p(z)\exp[-v(z)] - u_n(z)\exp[v(z)] + \frac{N_d(z) - N_a(z)}{n_i}\right], \tag{15}$$

$$\frac{d}{dz}\left\{D_n n_i \exp[v(z)]\frac{d u_n(z)}{dz}\right\} = R(z), \tag{16}$$

$$\frac{d}{dz}\left\{D_p n_i \exp[-v(z)]\frac{d u_p(z)}{dz}\right\} = R(z). \tag{17}$$

B. Discretization

Ge diodes with highly doped quasi-neutral regions are a challenging system for numerical simulations because two very different length scales coexist. One of them is the Debye length ℓ, relevant in the depletion layer, and the other one is the diffusion length L_D, relevant in the quasi-neutral regions. For $n,p \sim 10^{19}\,\mathrm{cm}^{-3}$, typical values of the Debye length are $\ell = 15\,\mathrm{nm}$, whereas $L_D > 3000\,\mathrm{nm}$. With such a severe mismatch, the need for a non-uniform discretization grid is apparent. The separation between two successive points is denoted as $h_j = z_{j+1} - z_j$. In terms of these quantities, it can be shown that the discrete version of Eqs. (15)–(17) is

$$-\frac{2\epsilon_{j+\frac{1}{2}}}{(h_j + h_{j-1})h_j}v_{j+1} - \frac{2\epsilon_{j-\frac{1}{2}}}{(h_j + h_{j-1})h_{j-1}}v_{j-1}$$
$$= -\left[\frac{2\epsilon_{j+\frac{1}{2}}}{(h_j + h_{j-1})h_{j+1}} + \frac{2\epsilon_{j-\frac{1}{2}}}{(h_j + h_{j-1})h_{j-1}}\right]v_j$$
$$+ \frac{4\pi e^2}{k_B T}[n_i u_{pj}\exp(-v_j) - n_i u_{nj}\exp(v_j) + N_{dj} - N_{aj}], \tag{18}$$

$$\frac{2n_i D_{n,j+\frac{1}{2}}}{(h_j + h_{j-1})h_j}B(v_j - v_{j+1})\exp(v_j)u_{n,j+1}$$
$$+ \frac{2n_i D_{n,j-\frac{1}{2}}}{(h_j + h_{j-1})h_{j-1}}B(v_j - v_{j-1})\exp(v_j)u_{n,j-1}$$
$$= \left[\frac{2n_i D_{n,j+\frac{1}{2}}}{(h_j + h_{j-1})h_j}B(v_j - v_{j+1})\exp(v_j)\right.$$
$$\left. + \frac{2n_i D_{n,j-\frac{1}{2}}}{(h_j + h_{j-1})h_{j-1}}B(v_j - v_{j-1})\exp(v_j)\right]u_{nj}$$
$$+ n_i^2[u_{nj}u_{pj} - 1](r_{j,\mathrm{SRH}} + B_{\mathrm{bim}}), \tag{19}$$

and

$$-\frac{2n_i D_{p,j+\frac{1}{2}}}{(h_j + h_{j-1})h_j}B(v_{j+1} - v_j)\exp(-v_j)u_{p,j+1}$$
$$- \frac{2n_i D_{p,j-\frac{1}{2}}}{(h_j + h_{j-1})h_{j-1}}B(v_{j-1} - v_j)\exp(-v_j)u_{p,j-1}$$
$$= -\left[\frac{2n_i D_{p,j+\frac{1}{2}}}{(h_j + h_{j-1})h_j}B(v_{j+1} - v_j)\exp(-v_j)\right.$$
$$\left. + \frac{2n_i D_{p,j-\frac{1}{2}}}{(h_j + h_{j-1})h_{j-1}}(Bv_{j-1} - v_j)\exp(-v_j)\right]u_{p,j}$$
$$- n_i^2[u_{nj}u_{pj} - 1](r_{j,\mathrm{SRH}} + B_{\mathrm{bim}}), \tag{20}$$

where for any function of position, $f_{j+\frac{1}{2}} = f\left(z_j + \frac{1}{2}h_j\right)$, and we introduce the Bernoulli generation function

$$B(y) = \frac{y}{\exp(y) - 1}. \tag{21}$$

This function appears following a method introduced by Scharfetter and Gummel[22] to avoid unphysical negative carrier concentrations that may arise because the discretization approximation

$n_{j+\frac{1}{2}} = \frac{1}{2}(n_{j+1} + n_j)$ is not sufficiently good near the edge of depletion layers, where the carrier concentrations change exponentially.[23] The numerical evaluation of $B(y)$ can also lead to instabilities that we eliminate by expanding the denominator to cubic order for $y < 1.5 \times 10^{-3}$.

We will also need to calculate the electric field $-dv/dz$ to account for TAT recombination and the Poole–Frenkel effect. This electric field is required at mesh points, not halfway between points. We then use[24]

$$-dv/dz|_j = -\frac{v_{j+1} - \left(\frac{h_j}{h_{j-1}}\right)v_{j-1} - \left[1 - \left(\frac{h_j}{h_{j-1}}\right)^2\right]v_j}{h_j\left(1 + \frac{h_j}{h_{j-1}}\right)}. \quad (22)$$

Each of the three equations (18)–(20) has the form

$$\alpha_{j+1}\eta_{j+1} + \alpha_{j-1}\eta_{j-1} = \alpha_j\eta_j + G_j(\eta_j) + f_j, \quad (23)$$

where η is a generic symbol for v, u_n, or u_p. The coefficients are summarized in Appendix B using dimensionless quantities defined below.

The three equations can be solved iteratively using a method proposed by Mayergoyz and co-workers.[21,25] The method consists of solving the equations

$$\Psi(\eta_j^{K+1}) \equiv \alpha_j\eta_j^{K+1} + G_j(\eta_j^{K+1}) - F_j^{K+1} = 0,$$
$$F_j^{K+1} = \alpha_{j+1}\eta_{j+1}^K + \alpha_{j-1}\eta_{j-1}^K - f_j^K, \quad (24)$$

where the superscript K indicates the order of the iteration. The first equation is a non-linear equation in η_j^{K+1}, which is solved itself iteratively, using, for example, the Newton method. This implies two iteration loops, one for K and one to solve the nonlinear equation. However, it makes no sense to spend computer time to solve the non-linear equation "exactly" if we are only finding an approximate solution for loop K. Therefore, we limit ourselves to the first iteration of the inner loop,[26] which leads to

$$\eta_j^{K+1} = \eta_j^K - \frac{\alpha_j\eta_j^K + G_j(\eta_j^K) - F_j^{K+1}}{\alpha_j + G_j'(\eta_j^K)}, \quad (25)$$

For the derivatives of G, the potential case is straightforward:

$$G'(v_j) = -\frac{4\pi e^2 n_i}{k_B T}\{u_{pj}\exp(-v_j) + u_{nj}\exp(v_j)\}. \quad (26)$$

For the current continuity equations, on the other hand, the derivatives are complex because r_j is itself a function of $u_{n,j}$ and $u_{p,j}$. We then use the so-called Seidman's modification[27] by writing

$$G_j(u_{n,j}^{K+1}) = n_i^2 u_{p,j}^K u_{n,j}^{K+1}(r_{j,\text{SRH}}^K + B_{j,\text{bim}}^K),$$
$$f_j^K = -n_i^2(r_{j,\text{SRH}}^K + B_{j,\text{bim}}^K), \quad (27)$$

and

$$G_j(u_{p,j}^{K+1}) = -n_i^2 u_{n,j}^K u_{p,j}^{K+1}(r_{j,\text{SRH}}^K + B_{j,\text{bim}}^K),$$
$$f_j^K = -n_i^2(r_{j,\text{SRH}}^K + B_{j,\text{bim}}^K). \quad (28)$$

This gives

$$G'(u_{n,j}^{K+1}) = n_i^2 u_{p,j}^K(r_{j,\text{SRH}}^K + B_{j,\text{bim}}^K),$$
$$G'(u_{p,j}^{K+1}) = -n_i^2 u_{n,j}^K(r_{j,\text{SRH}}^K + B_{j,\text{bim}}^K). \quad (29)$$

The final modification prior to numerical evaluation is to introduce normalized quantities. We define

$$\bar{\epsilon} = \min(\epsilon's),$$
$$\bar{N} = \max(N's),$$
$$D_{\max} = \max(D's), \quad (30)$$

and a length

$$\ell = \sqrt{\frac{\bar{\epsilon}k_B T}{4\pi e^2 \bar{N}}}. \quad (31)$$

This allows us to introduce a dimensionless coordinate x and dimensionless quantities ϵ', h', and D' such that

$$z = \ell x,$$
$$h_j = \ell h'_j,$$
$$\epsilon = \bar{\epsilon}\epsilon',$$
$$D = D_{\max}D'. \quad (32)$$

Similarly, we can define dimensionless recombination–generation coefficients as

$$r'_j = \frac{n_i\ell^2}{D_{\max}}r_j,$$
$$B'_{j,\text{bim}} = \frac{n_i\ell^2}{D_{\max}}B_{j,\text{bim}}. \quad (33)$$

A table with the coefficients in Eq. (23) using the normalized quantities just defined is shown in Appendix B.

C. Boundary conditions and initial guess

To explain the boundary conditions, we assume for concreteness that the p-layer is on the left of the diode and extends from $z_- = -W_p - d/2$ to $z_+ = W_n + d/2$, with ohmic contacts at both ends. Accordingly, equilibrium conditions and charge neutrality must prevail at both ends. If no external voltage is applied, equilibrium implies, according to Eq. (14), $u_n(z_-) = u_p(z_-) = u_n(z_+) = u_p(z_+) = 1$. Then, the charge neutrality condition on the left side is $N_a + n - p = 0$, so that Eq. (11) implies

$$v(z_-) = -\ln\left(\frac{N_a}{2n_i} + \frac{N_a}{2n_i}\sqrt{1 + \frac{4n_i^2}{N_a^2}}\right). \quad (34)$$

Similarly, we obtain

$$v(z_+) = \ln\left(\frac{N_d}{2n_i} + \frac{N_d}{2n_i}\sqrt{1 + \frac{4n_i^2}{N_d^2}}\right). \qquad (35)$$

Let us now consider the case when a voltage v_{app} is applied between the diode terminals. In that case, the boundary conditions for the potential are

$$v(z_-) = \frac{v_{app}}{2} - \ln\left(\frac{N_a}{2n_i} + \frac{N_a}{2n_i}\sqrt{1 + \frac{4n_i^2}{N_a^2}}\right), \qquad (36)$$

and

$$v(z_+) = -\frac{v_{app}}{2} + \ln\left(\frac{N_d}{2n_i} + \frac{N_d}{2n_i}\sqrt{1 + \frac{4n_i^2}{N_d^2}}\right). \qquad (37)$$

But since the carrier concentrations at the contacts are independent of the voltage at those points, then

$$\begin{aligned}
u_n(z_+) &= \exp\left[\frac{v_{app}}{2}\right], \\
u_n(z_-) &= \exp\left[-\frac{v_{app}}{2}\right], \\
u_p(z_+) &= \exp\left[-\frac{v_{app}}{2}\right], \\
u_p(z_-) &= \exp\left[\frac{v_{app}}{2}\right].
\end{aligned} \qquad (38)$$

Because the solution method used here is *globally* convergent,[21] any initial guess for the functions $\{u_n(z), u_p(z), v(z)\}$ leads eventually to the correct solution, but the time needed can vary considerably. We find that a reasonably fast solution is found by mimicking the depletion approximation. We assume that the initial potential $v_{initial}(z)$ is equal to $v(z_-)$ from z_- to $z_{left} = -d/2 - 3\ell$ and equal to $v(z_+)$ from $z_{right} = d/2 + 3\ell$ to z_+. For $z_{left} < z < z_{right}$, we linearly interpolate the potential values between $v(z_-)$ and $v(z_+)$. Similarly, we define a function $v_{app,initial}(z)$ such that it is equal to v_{app} for $z < z_{left}$, equal to $-v_{app}$ for $z_{right} < z$, and linearly interpolated between these values for $z_{left} < z < z_{right}$. With this definition, we take $u_{n,initial}(z) = \exp\left[-\frac{v_{app,initial}(z)}{2}\right]$ and $u_{p,initial}(z) = \exp\left[\frac{v_{app,initial}(z)}{2}\right]$.

D. External circuit

We assume the diode to be embedded in a circuit as depicted in Fig. 1. The externally applied voltage is V_{ext} and the externally measured current is I, which are not the same as the voltage V_d across the diode and the diode current diode I_d. The resistors in the figure account for the measuring circuit as well as for the physical characteristics of the diode itself. For example, non-ideal passivation of the sidewalls may lead not only to additional recombination/generation, as discussed below, but to a non-infinite value
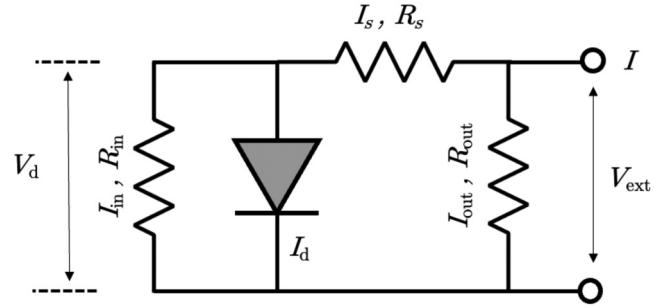

FIG. 1. Schematic diagram of the diode circuit leading to Eq. (40).

of R_{in}. By solving the circuit, we find that

$$V_d = (V_{ext} - I_d R_s)\left(\frac{R_{in}}{R_{in} + R_s}\right). \qquad (39)$$

The measured current is

$$I = \left(\frac{R_{in}}{R_{in} + R_s}\right)\left(\frac{V_{ext}}{R_{in}} + I_d\right) + \frac{V_{ext}}{R_{out}}. \qquad (40)$$

To find the diode current I_d, we must solve the non-linear equation

$$I_d = f\left[(V_{ext} - I_d R_s)\left(\frac{R_{in}}{R_{in} + R_s}\right)\right]. \qquad (41)$$

For an ideal diode, the solution is provided by the Lambert W-function, but in our case we need a numerical solution in which, for every iteration of the root-finding method, we must solve the semiconductor differential equations. The serial resistance can almost never be neglected, and in some cases, it may be increased intentionally to measure properties such as responsivity. Thus, accounting for its effect on the *I–V* curves is by far the most time-consuming aspect of the calculation, but it is essential to match experimental curves. We incorporate the differential equation solver into a root finding algorithm using Brent's method,[28] as implemented in the commercial package Igor Pro from Wavemetrics Inc.

Even with these complications, the time needed to compute a full *I–V* curve can be as short as a minute in a fast personal computer.

E. Recombination model details

1. Trap-assisted-tunneling and Poole–Frenkel effect

As indicated above, we assume that all defect-related recombination–generation processes can be described in terms of SRH. To account for trap-assisted tunneling, we follow the work of Hurkx *et al.*[29] and rewrite each of the summation terms in Eq. (6) as

$$R_t(z) = \frac{[n(z)p(z) - n_i^2]}{\frac{\tau_{pt}}{1 + \Gamma_{pt}}[n_t + n(z)] + \frac{\tau_{nt}}{1 + \Gamma_{nt}}[p_t + p(z)]}. \qquad (42)$$

Here, the recombination enhancement functions $\Gamma_{nt}(z)$ and $\Gamma_{pt}(z)$ account for trap-assisted tunneling (TAT) and the Poole–Frenkel effect, as described below.

Trap-assisted tunneling refers to carrier tunneling through the approximately triangular potential barrier in the presence of the electric field. We model the TAT contribution using the expressions derived by Hurkx et al.,[29]

$$\Gamma_{nt} = \frac{\Delta E_n}{k_B T} \int_0^1 \exp\left(\frac{\Delta E_{nt}}{k_B T} u - K_{nt} u^{3/2}\right) du,$$
$$\Gamma_{pt} = \frac{\Delta E_p}{k_B T} \int_0^1 \exp\left(\frac{\Delta E_{pt}}{k_B T} u - K_{pt} u^{3/2}\right) du,$$

$$(43)$$

with

$$K_{nt} = \frac{4}{3} \frac{\sqrt{2 m_\| (\Delta E_{nt})^3}}{e \hbar |\mathbf{E}|},$$
$$K_{pt} = \frac{4}{3} \frac{\sqrt{2 m_\| (\Delta E_{pt})^3}}{e \hbar |\mathbf{E}|},$$

$$(44)$$

where $|\mathbf{E}|$ is the magnitude of the electric field, $m_\|$ is the effective mass in the direction of transport, and $\hbar$ is the reduced Planck constant. The quantities ΔE_n and ΔE_p are the tunneling barriers and they are defined as (if we take $E_v = 0$, $E_c = E_g$)

$$\Delta E_n(z) = \begin{cases} E_g - E_t & \text{for } E_t \geq E_g - e[V(z_{\text{right}}) - V(z)], \\ e[V(z_{\text{right}}) - V(z)] & \text{for } E_t < E_g - e[V(z_{\text{right}}) - V(z)], \end{cases}$$

$$(45)$$

and

$$\Delta E_p(z) = \begin{cases} e[V(z) - V(z_{\text{left}})] & \text{for } E_t \geq e[V(z) - V(z_{\text{left}})], \\ E_t & \text{for } E_t < e[V(z) - V(z_{\text{left}})]. \end{cases}$$

$$(46)$$

These barriers may be lowered by the Poole–Frenkel effect,[30] caused by the presence of an electric field of magnitude $|\mathbf{E}|$. We can write this as

$$\Delta E_{PF} = \beta_{PF} |\mathbf{E}|. \tag{47}$$

For a Coulombic trap, one can show that $\beta_{PF} = \sqrt{4 e^3/\epsilon}$.

The barriers in Eqs. (45) and (46) are modified to new values, written as $\Delta E'_{n,p}$, which for a donor trap are given as

$$\Delta E'_n = \Delta E_n - \Delta E_{PF},$$
$$\Delta E'_p = \Delta E_p.$$

$$(48)$$

Similarly, for an acceptor trap, we obtain

$$\Delta E'_n = \Delta E_n,$$
$$\Delta E'_p = \Delta E_p - \Delta E_{PF}.$$

$$(49)$$

2. Perimetral recombination–generation

The diode model presented so far predicts that diodes that are identical except for their areas should have identical j–V curves. This is hardly ever observed in real life, the main reason being the presence of side wall recombination–generation that is not proportional to the area but to the diodes' perimeter. Good passivation can mitigate the effect, but not to the extent that perimetral recombination can be ignored if we seek a quantitative reproduction of the experimental I–V curves.

Unfortunately, incorporating sidewall recombination in a rigorous way requires a three-dimensional diode model. This, as indicated above, is incompatible with our stated goal of developing a fast, quantitative diode model that can be used to fit experimental curves. Therefore, we account for perimetral recombination–generation by developing a one-dimensional effective model. Starting from the fully three-dimensional semiconductor equations, we define average quantities by integrating over the diode area. These average quantities are only functions of the coordinate z and satisfy the one-dimensional equations (1)–(5). If we assume that perimetral defects are located within a distance δr of the diode surface, the averaging process for the SRH term corresponding to perimetral recombination gives

$$R_{\text{per}}(z) = \left(\frac{4}{D}\right) \frac{n(z)p(z) - n_i^2}{1/v_{n,\text{per}}[p_{\text{per}} + p(z)] + 1/v_{p,\text{per}}[n_{\text{per}} + n(z)]}. \tag{50}$$

Here, D is the device's diameter and we introduce perimetral recombination velocities $v_{n,\text{per}} = \delta r/\tau_{n,\text{per}}$, $v_{p,\text{per}} = \delta r/\tau_{p,\text{per}}$.

3. Recombination parameter choice

Our model contains one SRH term for each trap present. Unfortunately, a full independent identification of all such traps and their microscopic structure is not available. Therefore, our philosophy will be to use a model containing the smallest possible set of traps that is compatible with all available diode experimental data. We find that that this requires four trap levels. One trap is assumed to be the same one that appears in bulk Ge and represents the dominant recombination mechanism in Ge solar cells on Ge substrates. A second trap is associated with the above perimetral recombination. In addition to these traps, we find that for Ge-on-Si we need to include two additional dislocation-related traps. Even a simplified model like this contains 12 independent parameters (three per trap: energy, electron lifetime, and hole lifetime). If the trap parameters are known from independent work, they can be used unchanged in our simulations. This is the case, for example, for the bulk Ge recombination channels, whose parameters are presented in Appendix A. The traps related to dislocations and perimetral recombination, on the other hand, are not sufficiently well known and may be affected by growth and processing conditions. Rather than taking all of their parameters as adjustable, however, we make a number of plausible assumptions to limit the number of adjustable parameters to only two or at most three.

We assume the trap level for perimetral recombination is located in middle of the bandgap E_g, at an energy $E_g/2$ above the valence band edge. This is the trap energy that maximizes SRH recombination. For the dislocation-related traps, we assume that one of them is at the same midgap location $E_g/2$, while the other one appears at an energy $E_g/4$ above the valence band edge. There are several defect studies in Ge-on-Si as well as GeSn-on-Si, which provide evidence for shallow defects above the valence band edge at

energies close to $E_g/4$,[11,13,30–32] and we will show below that the presence of one such level is important for fitting the shape of the forward-bias I–V curves.

For each of the above traps, we need the electron- and hole-recombination lifetimes $\{\tau_{nt}, \tau_{pt}\}$ (or the surface recombination velocities $\{v_{n,\mathrm{per}}, v_{p,\mathrm{per}}\}$ in the case of perimetral recombination) to compute the corresponding R_{SRH} term. For the midgap dislocation-related trap, we assume that electron- and hole-recombination lifetimes are the same and inversely proportional to the dislocation density ρ_D,

$$\tau_{n,\mathrm{mid}} = \tau_{p,\mathrm{mid}} = \frac{1.2}{\rho_D}\left(\frac{\mathrm{s}}{\mathrm{cm}^2}\right). \tag{51}$$

A discussion of this choice is given in Appendix A. We also assume that the shallow level recombination parameters are

$$\tau_{n,\mathrm{shallow}} = \tau_{p,\mathrm{shallow}} = \frac{\tau_{n,\mathrm{mid}}}{r_{\mathrm{md}}} = \frac{\tau_{p,\mathrm{mid}}}{r_{\mathrm{md}}}, \tag{52}$$

where r_{md} is a number that we expect to be approximately constant among different Ge-on-Si samples if our defect model is physically valid. In fact, we find that the choice $r_{\mathrm{md}} = 75$ leads to good agreement with experiment in most cases. For this value of r_{md}, the midgap and shallow dislocation traps make comparable contributions.

Using the final assumption $v_{n,\mathrm{per}} = v_{p,\mathrm{per}}$, we end up with essentially a two-parameter recombination model (a three-parameter model if we take r_{md} as adjustable) in which the main adjustable parameters are the dislocation density and the surface recombination velocity.

It is apparent that some of the assumptions made in our trap models are crude and ad hoc, but more realistic accounts require very detailed defect studies that are simply not available at this time. Since the model presented here can in principle quantify the impact of the different traps on the I–V characteristics, we hope that it will stimulate further research on traps that are important for device performance.

III. MODEL PREDICTIONS

Before attempting to fit real experimental data, we show some model predictions that illustrate the perils of "naïve" studies based on analytical approximations, as described in the introduction, and also show how the different model parameters affect the predicted I–V curves.

A. Electric field effects

Figure 2 shows a few calculated electric fields for a typical *pin* structure. The accurate calculation of these fields is important, among other considerations, because they modify recombination via the TAT and Poole–Frenkel effects. We consider the cases in which the *i*-layer is truly intrinsic and those in which there is some residual carrier concentration. Even in the purely intrinsic case, the calculated electric field is significantly different from the depletion approximation analytical prediction near the n/i and p/i interfaces, as is well known.[18] If residual doping is present, the electric field is drastically changed, and for this situation there are no simple analytical
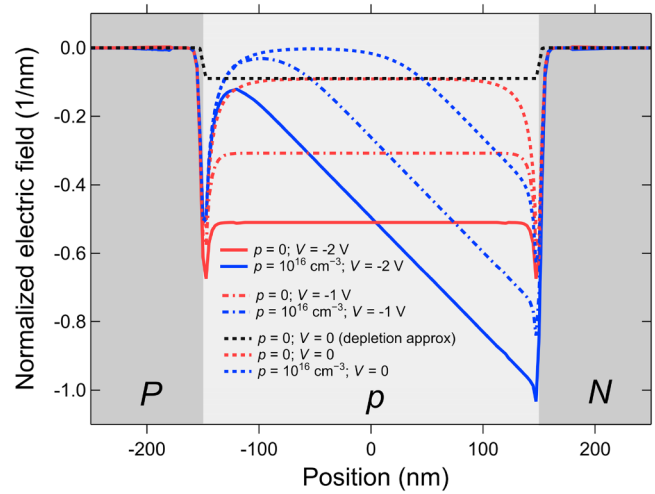
FIG. 2. Calculated electric fields in a *pin* diode ($P = N = 10^{19}$ cm^{-3}) at three different applied voltages. Solid lines are for $V_{\mathrm{app}} = -2$ V, dash-dotted lines for for $V_{\mathrm{app}} = -1$ V, and dotted lines for $V_{\mathrm{app}} = 0$. At each voltage, the red line corresponds to a perfectly intrinsic layer and the blue line to an intrinsic layer with a residual doping concentration $p = 10^{16}$ cm^{-3}. The black dotted line is the depletion approximation result for $V_{\mathrm{app}} = 0$.

approximations that can be used. These simulations underscore the need for a fully numerical solution of the semiconductor equations.

B. Voltage dependence of reverse-bias current

An important aspect of the experimental I–V curves in Ge-on-Si diodes is the relatively strong voltage dependence of the reverse-bias current. Figure 3 shows how the TAT and Poole–Frenkel mechanisms affect the slope of the reverse-bias curve. When residual doping is present, Fig. 2 shows that in the nominally intrinsic layer there is a region near the i/n interface (for hole residual carriers) with higher electric fields compared to the case of no residual doping, and a region with very low electric fields that decreases as the reverse-bias voltage increases. This causes the strongest voltage dependence of the reverse-bias curve, as shown by the red dash-dotted curve in Fig. 3. Because of this dependence, the amount of residual doping is a sensitive and critical parameter to fit experimental I–V curves.

C. Trap-energy dependence of the forward-bias current

Figure 4 shows calculated j–V curves assuming different energies for the trap levels associated with dislocations. The dislocation densities for the two simulations have been adjusted to match the reverse-bias curves. Since the curves are very similar in this range, it is possible to fit experimental data with very different ratios of midgap to shallow traps. On the other hand, in the forward-bias regime, the curves look very different, and therefore the forward-bias regime is sensitive to the choice of trap level, as anticipated above.
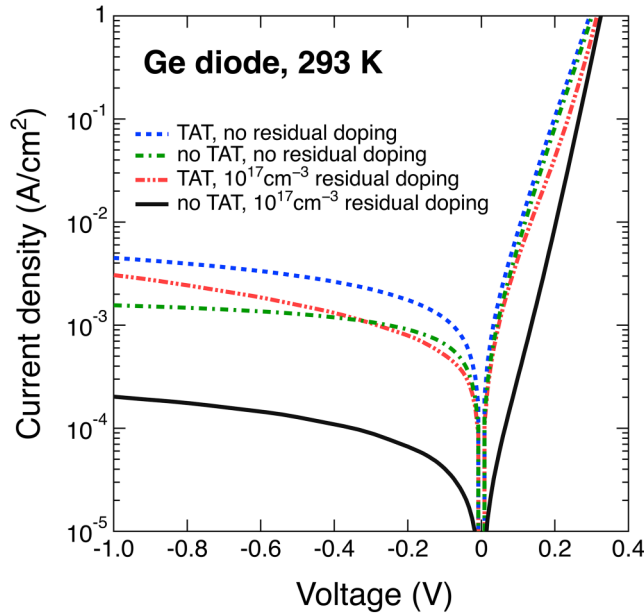
FIG. 3. Calculated j–V curves for a Ge *PiN* diode ($P = N = 10^{19}$ cm^{-3}) with a dislocation density $\rho_D = 10^7 cm^{-2}$. If there is no residual doping in the intrinsic layer, the dash-dotted green and dotted blue lines show the enhancement of the reverse-bias current due to TAT processes. In the presence of residual doping in the intrinsic layer ($p = 10^{17}$ cm^{-3}) there is a significant reduction of the reverse-bias current if TAT is absent (solid black line), but including TAT enhances the reverse-bias current and increases its slope.
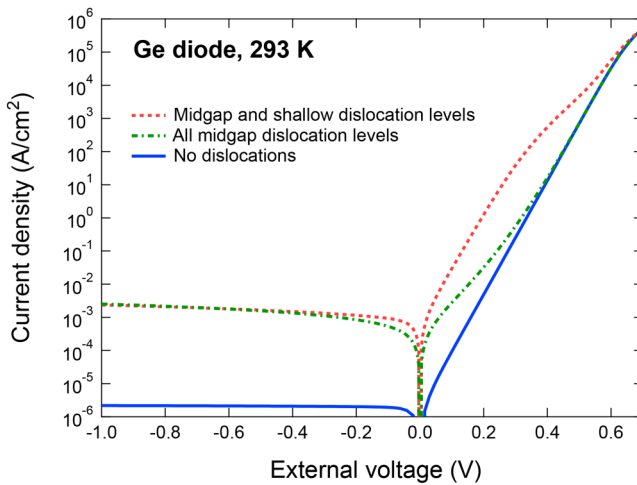
FIG. 4. Calculated j–V curves for a Ge *PiN* diode ($P = N = 10^{19}$ cm^{-3}). The solid blue line is the prediction for the case where there are no dislocation defects. The green dash-dotted curve is the prediction if all dislocation-related traps are at midgap, while the red dotted curve assumes the presence of shallow dislocation traps. The dislocation densities were adjusted to match the reversebias curves in order to highlight the differences under forward bias.
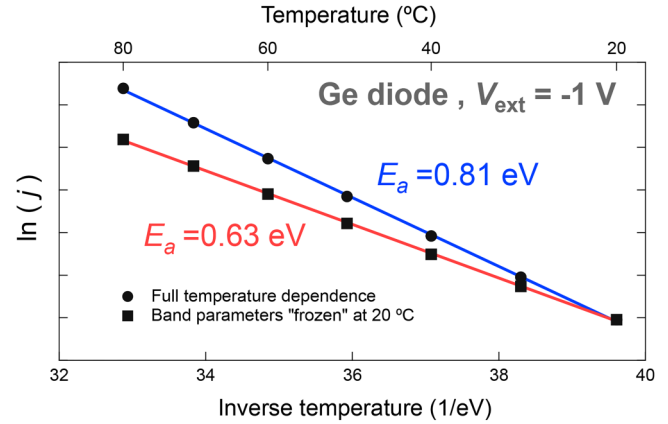
FIG. 5. Arrhenius plots of the predicted reverse-bias current at -1 V for a Ge *pin* diode containing no defects. Circles correspond to the full calculation, which gives an activation energy $E_a = 0.81$ eV. Squares correspond to the same calculation but keeping the electronic structure parameters artificially held at 20 °C. The activation energy is then reduced to $E_a = 0.63$ eV, which is very close to the bandgap $E_g = 0.66$ eV.

D. Temperature dependences

Figure 5 shows Arrhenius plots from j–V curves calculated with our model for the case of no defects, when the reverse-bias current is purely diffusive. In this case, an elementary analysis shows that the activation energy E_a is the material's bandgap $E_g = 0.66$ eV. However, a fit of the Arrhenius plot gives a much higher activation energy $E_a = 0.81$ eV. We recover an activation energy very close to the bandgap value if we "freeze" the band structure parameters, mobilities, and lifetimes to their values at 20°C. Similarly, we show in Fig. 6 the same calculation but for a case when the reverse-bias current is dominated by midgap defects, in which case the "expected" activation energy is $E_a = E_g/2$. Again, we obtain a result very close to this value ($E_a = 0.32$ eV) when we "freeze" the electronic and transport parameters at 20°C, but when the full temperature dependences are included, the predicted activation energy is $E_a = 0.42$ eV, a considerably higher value. These results suggest that simple Arrhenius plots of experimental data are a poor way to determine the relevant trap energies. This has already been recognized in the literature, although many authors rely on such methods for their analysis. Modified methodologies have been proposed to study the effect of traps on the diode current.[33] Our model suggests a complementary and potentially more powerful approach, which is to compare the predicted and observed temperature dependence of the reverse-bias current and adjust the trap energies until a good match between theory and experiment is obtained.

IV. EXPERIMENTAL DATA FITS

From our discussion of the recombination model, we limit the number of adjustable parameters to at most three: ρ_D, $v_{n,\text{per}} = v_{p,\text{per}}$, and possibly r_{md}. In addition, the residual doping in the intrinsic layer and the values of the effective circuit resistances
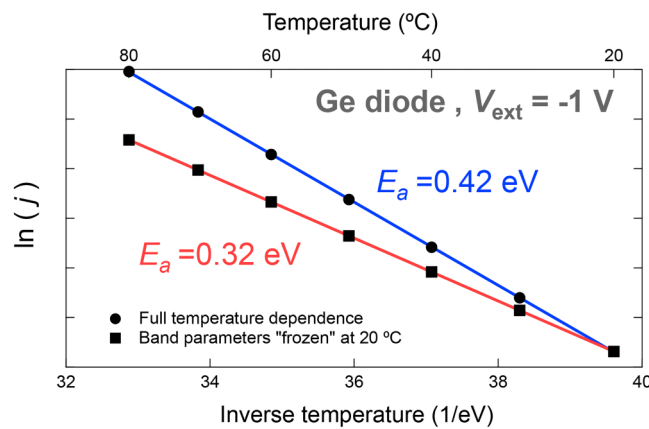
FIG. 6. Arrhenius plots of the predicted reverse-bias current at -1 V for a Ge *pin* diode for which the current is dominated by midgap defects. Circles correspond to the full calculation, which gives an activation energy $E_a = 0.42$ eV. Squares correspond to the same calculation but keeping the electronic structure parameters artificially held at 20 °C. The activation energy is then reduced to $E_a = 0.32$ eV, which is very close to $E_g/2$.

in Fig. 1 are potentially additional adjustable parameters. This is already a fairly limited set. Furthermore, we can take advantage of the fact that the parameters are largely independent because they have a strong influence on different aspects of the *I–V* curve. For example, the serial resistance is critical for determining the forward-bias curve, and the surface recombination velocity is solely responsible for the observation of different *j–V* curves from diodes with different areas but otherwise identical. As to the parallel resistances in Fig. 1, good *I–V* curve fits are usually obtained by setting $R_{in} = R_{out} = \infty$. If the parallel resistances cannot be entirely ignored, they can be determined by adjusting the *I–V* curves as a function of temperature, as we will demonstrate below.

While there are numerous publications reporting *I–V* curves for Ge-on-Si diodes, many of those articles fail to report these curves in sufficient detail and/or do not provide some parameters that our model takes as given, such as layer thicknesses and doping levels. We also note that strain modifies the band structure and affects the *I–V* curves indirectly. Our model accounts for some of those effects (see Appendix A) but strain levels are not always reported in the literature. We show next a few examples from Ge-on-Si samples, grown following different methods, for which sufficient data are available for meaningful modeling.

A. Two-step growth method

Perhaps the most popular approach to grow low-defect Ge on Si consists of a two-step approach in which an initiation Ge layer is deposited at relatively low temperatures around 400 °C followed by a growth temperature ramp up to about 670 °C.[35] Complete Ge homostructure *pin* diodes fabricated using this method were characterized by Colace *et al.*[36] Figure 7 shows the *j–*V curve for $D = 80 \, \mu m$ device. Since the current density is about the same for all device sizes, we set the surface recombination velocities equal to
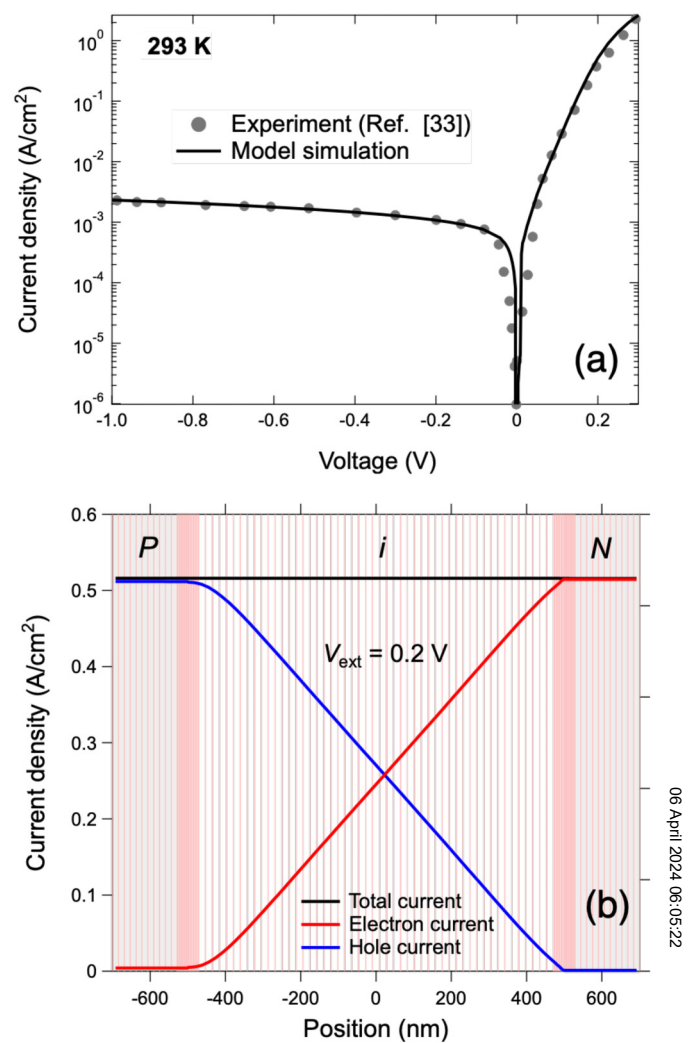
FIG. 7. (a) Experimental *j–*V curve for a $D = 80 \, \mu m$ *pin* diode from Colace *et al.* (Ref. 34). The solid line is a simulation assuming no perimetral recombination, a dislocation density $\rho_D = 8 \times 10^6 \, cm^{-2}$, a mid-shallow ratio $r_D = 100$, and a serial resistance $R_s = 400 \, \Omega$. (b) Details of the numerical simulation to compute the diode current. The vertical lines show the position of the 86 points in the selected integration mesh. The region with a high density of points corresponds to the transitions from *P* to *i* and from *i* to *N*. The lines show the electron, hole, and total currents in the structure for an applied voltage of 0.2 eV. This illustrates the degree of convergence of the calculation.

zero for our sample modeling. The solid line in Fig. 7(a) shows our fit using a dislocation density $\rho_D = 8 \times 10^6 \, cm^{-2}$ and $r_D = 100$. We assume no residual doping in the intrinsic layer and a serial resistance of 400 Ω. We see that the fit is in excellent agreement with the data. The dislocation density is within the range reported for this type of growth, and the fact that a good fit is obtained with no residual doping is consistent with SIMS measurements that show dopant densities below $2 \times 10^{14} \, cm^{-3}$.

Balbi et al.[36] studied the temperature dependence of the I–V curves in samples similar to those described in Ref. 36. For $V_{ext} = -1$ V, their experimental activation energy is $E_a = 0.64$ eV, which they attributed to a significant role of diffusion. This is hard to understand because the observed reverse-bias currents are three orders of magnitude higher than those our model predicts for a diode without dislocation defects. On the other hand, our simulations, as shown in Sec. III D, indicate that the temperature dependence of the band structure leads to effective activation energies that are higher than those expected from simple models so that the value $E_a = 0.64$ eV does not necessarily imply a diffusion-dominated regime. In fact, our model predicts in this case an activation energy $E_a = 0.52$ eV, entirely due to the defect levels. This value is not in excellent agreement with the experimental measurement, but it is clearly higher than $E_g/2$. Another discrepancy between model and experiment is that Balbi et al. find a strong voltage dependence of the activation energy, with a significant decrease from $V_{ext} = -1$ V to $V_{ext} = -3$ V, for which the activation energy is found to be $E_a = 0.32$ eV. We find a much weaker voltage dependence from $E_a = 0.52$ eV at $V_{ext} = -1$ V to $E_a = 0.50$ eV at $V_{ext} = -3$ V.

B. Germanium-on-insulator

Son and co-workers[14] have published a detailed study of *pin* photodetectors grown on Ge-on-insulator. They consider samples with high- and low-dislocation densities, the latter obtained by annealing. They also provide data on size and temperature dependence, which allow for a more complete deployment of a simulation model.

Figure 8 shows experimental data and model fits for samples with measured high and low threading dislocation densities $\rho_D = 5.2 \times 10^8$ cm^{-2} and $\rho_D = 3.2 \times 10^6$ cm^{-2}, respectively, and different sizes. Our model calculations reproduce the experimental I–V curves using $\rho_D = 1.1 \times 10^9$ cm^{-2} and $\rho_D = 1.6 \times 10^6$ cm^{-2},
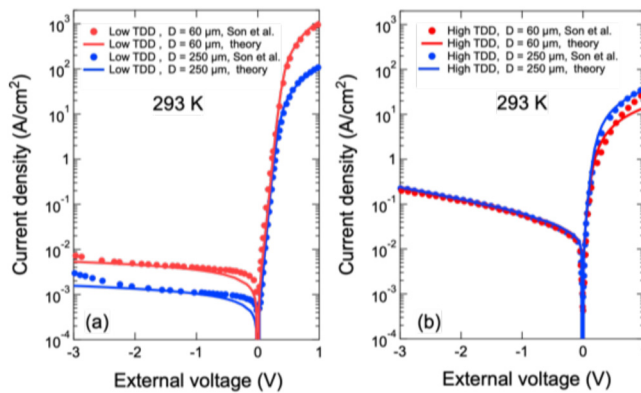
FIG. 8. Experimental j–V curves for *pin* diodes of different diameters D and dislocation densities ρ_D from Son et al. (Ref. 14). Dots are experimental data and solid lines are simulations. (a) Diodes with low-dislocation levels, fit with $\rho_D = 3.2 \times 10^6$ cm^{-2} and $v_p = v_n = 3.4 \times 10^4$ cm/s; (b) Diodes with high-dislocation levels, fit with $\rho_D = 1.1 \times 10^9$ cm^{-2}, $v_p = v_n = 3.4 \times 10^4$ cm/s, and a residual intrinsic layer doping $p = 1.5 \times 10^{17}$ cm^{-3}.

within a factor of 2 in both cases. Using perimetral recombination velocities $v_p = v_n = 3.4 \times 10^4$ cm/s, we are able to match the size dependence of the reverse-bias current in the low-dislocation samples and reproduce the lack of such dependence in the highly dislocated samples. On the forward-bias region, we use series resistances of 12 and 15 Ω, respectively, for the $D = 250$ and $D = 60 \, \mu$m devices with low levels of dislocations. For the highly dislocated diodes, we find that the best fit is obtained with a serial resistance of 45 Ω for the $D = 250 \, \mu$m diode, but as high as 2 kΩ for the $D = 60 \, \mu$m. We see that for this sample the fit at the highest forward bias is not nearly as good, suggesting some contact anomaly in this particular diode.

The most important qualitative difference between the high- and low-dislocation diodes is the observation of a much stronger voltage dependence of the reverse-bias current in the former. We reproduce this behavior by assuming some residual doping in the intrinsic layer of the highly dislocated materials; the best fit being obtained using $p = 1.5 \times 10^{17}$ cm^{-3}. On the other hand, in the low-dislocation diodes, there is a significant increase in the current for reverse biases beyond 2 eV. This behavior is not reproduced by our model at this point and may be due to BTBT effects.

As to the temperature dependence, an Arrhenius plot of the experimental reverse-bias current at -1 V gives for the high-dislocation samples an activation energy $E_a = 0.35$ eV, while our simulations give $E_a = 0.38$ eV, in very good agreement with experiment. On the other hand, for the low-dislocation diodes, our model predicts slightly lower activation energies of $E_a = 0.34$–0.35 eV, but the Arrhenius plots of the experimental data have a significant non-linear component.

C. Low-temperature Ge precursors

Kouvetakis and co-workers have introduced several low-temperature advanced precursors for the growth of Ge-on-Si that eliminate the need for a two-step process and are compatible with several doping precursors, making it possible to grow *in situ* complete diode structures with box-like doping profiles.[17, 38–42] The availability of these materials has enabled significant advances in our basic understanding of doped Ge materials, including the study of incomplete ionization,[43] the physics of the doping dependence of the lattice parameter,[44] the observation of Pauli-blocking singularities in the dielectric function of highly doped n-Ge,[45, 46] and the advancement of metrology efforts for the determination of carrier concentrations using Hall and optical measurements.[47]
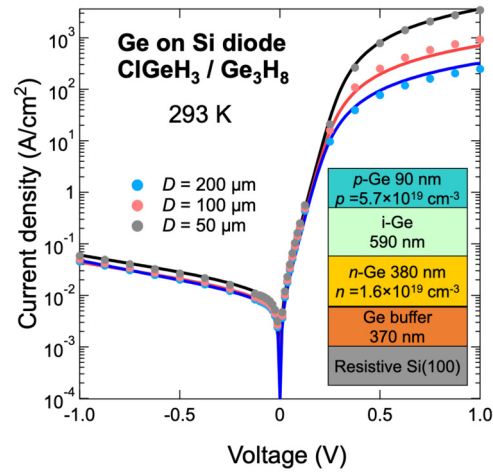
Figure 9 shows selected I–V curves for a device grown by combining Gas Source Molecular Epitaxy (GSME) and Ultrahigh Vacuum Chemical Vapor Deposition (UHV-CVD). Both capabilities are described elsewhere.[48,49] First, a Ge buffer layer, the n-type layer, and the intrinsic layer are grown by GSME on a Si (100) substrate using the Ge$_4$H$_{10}$ and P(SiH$_3$)$_3$ precursors at a temperature of 370 °C. The use and advantages of Ge$_4$H$_{10}$ for the growth of Ge were first discussed by Xu et al.[48] The sample is then transferred to the UHV-CVD system, where the final p-layer is grown using the Ge$_3$H$_8$ and B$_2$H$_6$ precursors. A very good simultaneous fit of the j–V curves is obtained using $\rho_D = 10^8$ cm^{-2}, $r_{md} = 75$, an intrinsic layer unintentional doping of $p = 9.5 \times 10^{17}$ cm^{-3}, $v_p = v_{n-} = 10^6$ cm/s, and $R_s = 3\Omega$, $R_{in} = \infty$, and $R_{out} = \infty$.
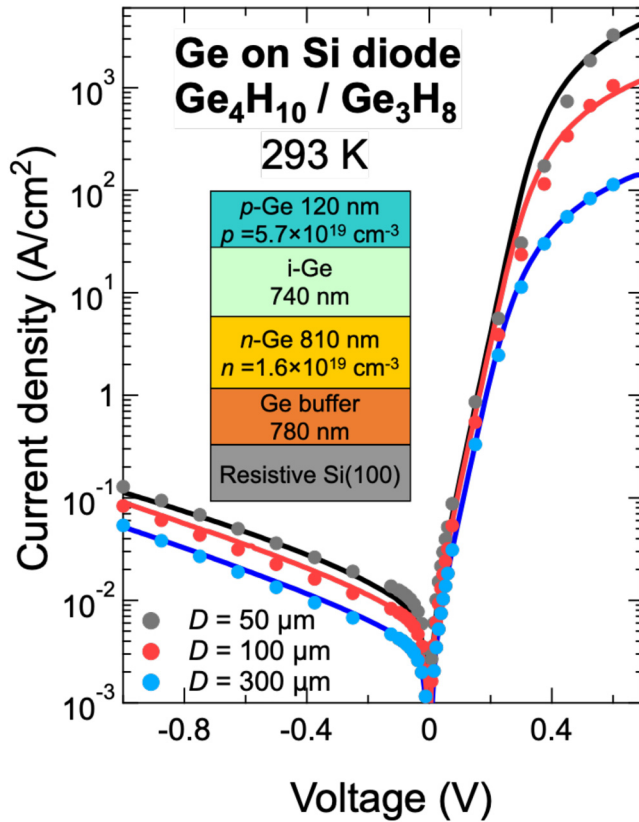
FIG. 9. Experimental j–V curve for a Ge pin diode on Si grown using heavy polygermanes and *in situ* doping. The solid lines are the experimental curves and the dots correspond to the theoretical simulation. The inset shows the schematics of the sample.

FIG. 10. Experimental j–V curve for a Ge pin diode on Si grown using ClGeH$_3$ and Ge$_3$H$_8$ and *in situ* doping. The solid lines are the experimental curves and the dots correspond to the theoretical simulation. The schematic diagram on the right shows the sample design.

Figure 10 shows the I–V characteristics of a diode that is structurally similar to the previous diode except that the Ge$_4$H$_{10}$ precursor has been replaced with chlorogermane ClGeH$_3$, a new Ge-source recently introduced by our group.[42] A good simultaneous fit of the j–V curves is obtained using $\rho_D = 5 \times 10^8$ cm^{-2}, $r_{md} = 75$, an intrinsic layer unintentional doping of $p = 4 \times 10^{17}$ cm^{-3}, $v_p = v_n = 4 \times 10^5$ cm/s, and $R_s = 8.6\Omega$, $R_{in} = \infty$, and $R_{out} = \infty$.

While good fits are obtained assuming infinite parallel resistances—attributing all the observed diameter dependence to perimetral recombination, as we did in Figs. 9 and 10—it is difficult as a practical matter to rule out the presence of a finite parallel resistance that is proportional to $1/D$, as discussed in Sec. II E 2. Furthermore, even if one accepts that the diameter dependence is fully accounted for by perimetral recombination, the presence of a finite, diameter independent parallel resistance would affect the slope of the reverse-bias curve in a way that is hard to disentangle from the effect of residual intrinsic layer doping combined with TAT processes, as discussed in Sec. III B. For an unambiguous identification of the possible parallel resistance contributions, a study of the temperature dependence of the I–V curve is very useful, as we show next.

Figure 11 presents the I–V characteristics of a diode grown entirely in the GSME system using Ge$_4$H$_{10}$ as the Ge precursor. In this case, the n-type layer, doped with P(SiH$_3$)$_3$, was grown directly on Si without buffer layers, and the dopant for the top p-type layer was Ga hydride [D$_2$GaN(CH$_3$)$_2$]$_2$ diluted in H$_2$, as described in Ref. 50.

The diode in Fig. 11 displays lower values of the reverse-bias current at room temperature compared to those in Figs. 9 and 10. This implies that the resistances R_{in} and R_{out} in Fig. 1 must be both greater than 50 MΩ for the measured current not to be affected by their values. For smaller values, the current through the resistors must be accounted for by the model. But as the temperature increases, the diode current increases exponentially and eventually becomes completely dominant over the current through the parallel resistors. Therefore, the diode parameters can be obtained by fits at the higher temperatures, and the parallel resistance values can then be adjusted to improve the fit of the low-temperature I–V curves. This procedure has led to the excellent agreement shown in Fig. 11(a), using $\rho_D = 7.3 \times 10^7$ cm^{-2}, $r_{md} = 75$, an intrinsic layer unintentional doping of $p = 5 \times 10^{16}$ cm^{-3}, $R_s = 15\Omega$, $R_{in} = 4$ MΩ, and $R_{out} = \infty$. An equally good fit is obtained by setting $R_{in} = \infty$ and adjusting R_{out}. The agreement can be made even better by minor tweaks in the parameters for each of the curves, or by allowing for small deviations in the target temperature within the error of the measurement. Figure 11(b) shows all measured (gray squares) and calculated (red circles) current densities at -1 V as a function of temperature. We see that the agreement between model and experiment is quite remarkable. The blue triangles in the figure show a calculation with the same parameters except that we take $R_{in} = \infty$. A comparison of the red circle and blue triangle calculations clearly illustrates the aforementioned impact of a non-infinite parallel resistance: at the lowest temperatures, there is a clear

06 April 2024 06:05:22
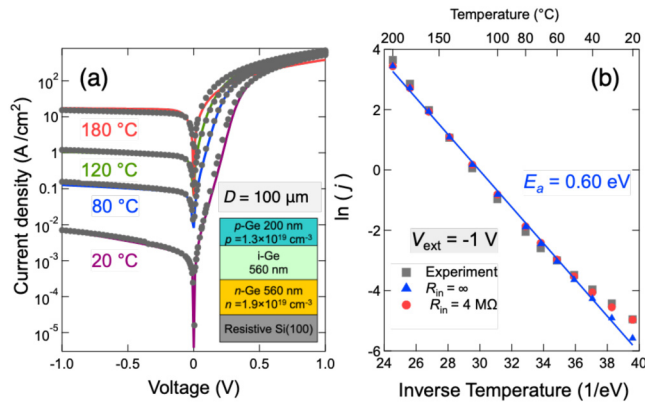
FIG. 11. (a) Selected experimental j–V curves for a Ge pin diode on Si grown entirely in a GSME reactor. The lines are the experimental data and the dots the model predictions using exactly the same parameters $\rho_D = 7.3 \times 10^7\ \text{cm}^{-2}$, $r_{md} = 75$, an intrinsic layer unintentional doping of $p = 5 \times 10^{16}\ \text{cm}^{-3}$, $R_s = 15\ \Omega$, $R_{in} = 4\ \text{M}\Omega$, and $R_{out} = \infty$. (b) Grey squares: Arrhenius plot of the experimental reverse-bias current at all temperatures. Red dots: model predictions with the above parameters. Blue triangles: model predictions with the same parameters except that we set $R_{in} = \infty$. The solid blue line is a linear fit that gives an activation energy $E_a = 0.60\ \text{eV}$. This is close to the material's bandgap, but the reverse-bias current is completely dominated by the defect contribution.

deviation between triangles and circles, but at higher temperatures the two predictions are virtually identical. These results suggest that some reported deviations from the linear behavior expected in an Arrhenius plot may be simply due to the presence of a non-infinite parallel resistance that has not been properly accounted for. On the other hand, even the blue triangles show some deviation from a purely linear behavior, clearly reflecting the influence of the non-exponential temperature dependence of several material parameters, as discussed above. Nevertheless, we have fit the prediction with a straight line and find an activation energy $E_a = 0.60\ \text{eV}$. This suggests a diffusion-dominated current, but, as indicated in Sec. III D, the activation energies obtained from such an exercise cannot be easily interpreted in those terms. In fact, the model calculation shows that at all temperatures, the reverse-bias current is dominated by the defect contribution.

V. CONCLUSIONS

We have presented a practical yet realistic model for the I–V characteristics of Ge-on-Si pin diodes. The model can reproduce I–V curves in the literature from a variety of sources by adjusting a very limited number of parameters and should therefore be useful for systematic studies aimed at improving the performance of such diodes. Extensions to GeSn and SiGeSn materials are straightforward and only require new sets of material parameters instead of those presented in Appendix A, which apply to Ge. Heterostructure diodes can also be included with minor modifications. We will also show in a forthcoming paper how the model can be combined with rigorous optical calculations to predict the

optical responsivity from Ge, GeSn, and SiGeSn pin diodes without the need of adjustable parameters such as collection efficiencies.

While the agreement between calculated and experimental I–V curves is excellent, mixed results are obtained for the temperature dependence of these curves. There are some obvious reasons why the predicted temperature dependences may disagree with experiment. For example, we assume the trap levels to track the temperature dependence of the bandgap. Different results are obtained in the opposite limit in which the trap level is assumed to lie at a fixed energy relative to one of the band edges. Furthermore, we take the recombination lifetimes for the dislocation-related traps to be temperature-independent for lack of any direct measurement, although there is ample evidence that other recombination lifetimes in the system have their own temperature dependence. From this perspective, a failure to reproduce the temperature dependence of the I–V curves would not necessarily imply that there is a fundamental flaw in our model, but simply reflect our incomplete knowledge of the fundamental physics associated with recombination–generation processes. On the other hand, the excellent agreement between modeled and experimental temperature dependence for some of the modeled diodes (for example, Fig. 11) is hard to explain if we are omitting some important contribution to the temperature dependence. In fact, it suggests that better control of the experimental conditions may be necessary to carry out these critical measurements and that fits that do not account for the parallel resistances may not converge well or lead to erroneous conclusions.

AUTHOR DECLARATIONS

Conflict of Interest

The authors have no conflicts to disclose.

Author Contributions

Matthew A. Mircovich: Data curation (equal); Formal analysis (equal); Investigation (equal); Validation (equal); Visualization (equal); Writing – original draft (equal); Writing – review & editing (equal). **John Kouvetakis:** Conceptualization (lead); Data curation (equal); Formal analysis (equal); Funding acquisition (equal); Investigation (equal); Methodology (equal); Project administration (equal); Resources (equal); Software (equal); Supervision (equal); Validation (equal); Writing – original draft (supporting); Writing – review & editing (equal). Conceptualization (lead); Data curation (equal); Formal analysis (equal); Funding acquisition (lead); Investigation (equal); Methodology (equal); Project administration (lead); Resources (lead); Software (equal); Supervision (lead); Validation (equal); Writing – original draft (equal); Writing – review & editing (equal).

DATA AVAILABILITY

The data that support the findings of this study are available within the article.

APPENDIX A: MODEL PARAMETERS

1. Lattice parameter

The temperature dependence of the lattice parameters of both Si and Ge is needed to compute thermal stresses on epitaxial films and to evaluate the temperature dependence of the momentum matrix elements, as discussed below. Experimentally, the temperature-dependent lattice parameter can be computed from thermal expansivity measurements. In Ref. 51, we present a physically motivated model that reproduces these experimental data for Si, Ge, and α-Sn. However, since the expressions derived require numerical integrations to obtain the desired lattice parameter, we take a more practical route here. In the case of Si, we fit the experimental thermal expansion data from Ibach,[52] which extend from 10 to 800 K, with an eight-order polynomial. This leads to

$$a_{\mathrm{Si}}(T) = a_{0,\mathrm{Si}} \exp\left(\sum_{m=1}^{8} \frac{1}{m}\alpha_m T^m\right), \qquad (A1)$$

with $\alpha_1 = 3.772\,92 \times 10^{-7}\,\mathrm{K}^{-1}$, $\alpha_2 = -2.421\,69 \times 10^{-8}\,\mathrm{K}^{-2}$, $\alpha_3 = 1.841\,59 \times 10^{-10}\,\mathrm{K}^{-3}$, $\alpha_4 = 1.752\,44 \times 10^{-13}\,\mathrm{K}^{-4}$, $\alpha_5 = -3.333\,74 \times 10^{-15}\,\mathrm{K}^{-5}$, $\alpha_6 = 8.745\,87 \times 10^{-18}\,\mathrm{K}^{-6}$, $\alpha_7 = -9.356\,95 \times 10^{-21}\,\mathrm{K}^{-7}$, and $\alpha_8 = 3.663\,27 \times 10^{-24}\,\mathrm{K}^{-8}$. We also chose $a_0 = 5.4297$ Å to match our measurements of bulk Si wafers at room temperature.

For Ge, the available thermal expansion data only reach 300 K, but *ab initio* calculations that extend beyond this temperature and agree with the experimental data are available.[53] We have then first adjusted an expression similar to Eq. (A1) to the experimental data, and then fit the resulting $a(T)$ curve with an empirical expression of the form

$$a_{\mathrm{Ge}}(T) = a_{0,\mathrm{Ge}} + A\left[1 + \frac{2}{\exp\left(\dfrac{\Theta}{T}\right) - 1}\right]. \qquad (A2)$$

The fit parameters are $A = 6.5741 \times 10^{-3}$ K and $\Theta = 355.14$ K. The zero-temperature value was chosen as $a_{0,\mathrm{Ge}} = 5.645$ Å to match literature values at room temperature. With these parameters, we obtain a good agreement with the theoretical predictions above 300 K.

2. Electronic and optical parameters

a. Bandgaps

The most important parameter is the fundamental indirect gap, for which we use

$$E_g(T) = E_g(0) - \frac{\alpha T^2}{\beta + T}, \qquad (A3)$$

with $E_g(0) = 0.7440$ eV, $\alpha = 4.956 \times 10^{-4}$ eV/K, and $\beta = 216.8$ K, as discussed in Ref. 19.

For the direct bandgap, we use Eq. (27) in Ref. 54, with parameters given in that paper.

b. Effective masses

The valley with minimum at the *L*-point of the Brillouin zone where electron carriers reside in Ge is characterized by a longitudinal mass m_l (corresponding to the $\langle 111 \rangle$ directions) and a transverse mass m_t. The longitudinal mass is taken as $m_l = 1.58m_0$, where m_0 is the free electron mass. It is assumed to be independent of temperature.[55] Expressions for the transverse mass as a function of temperature are given in Appendix B of Ref. 46. At 20 °C, the corresponding value is $m_l = 0.0786m_0$. For calculations involving TAT tunneling, we need effective masses in the direction of the current, which we indicate with a subscript "c." For our diodes, the relevant direction is [001]. It is then easy to show that the corresponding electron mass is

$$\frac{1}{m_{\parallel,c}} = \frac{1}{3}\left(\frac{2}{m_t} + \frac{1}{m_l}\right). \qquad (A4)$$

At the Γ-minimum of the conduction band, the dispersion is assumed to be isotropic, so there is no distinction between directions, and the effective mass is given by

$$\frac{m_0}{m_c} = 1 + \frac{2P^2}{3m_0}\left(\frac{2}{E_0} + \frac{1}{E_0 + \Delta_0}\right), \qquad (A5)$$

where E_0 is the direct bandgap and Δ_0 is the valence band spin–orbit splitting at the Γ-point. The quantity P is the momentum matrix element at the Γ-point. Using a 30-band $k \cdot p$ code,[56] we have studied the effect of distant bands on the effective mass m_c, and we find it is negligible. Therefore, the use of Eq. (A5) is perfectly justified. Using experimental values for the effective mass and the bandgap parameters from Aggarwal,[57] we find $\frac{P^2}{2m_0} = 12.299$ eV at 30 K. The spin–orbit splitting is taken as $\Delta_0 = 0.287$ eV and as temperature-independent.[58] The temperature dependence of the effective mass is then determined by the temperature dependence of E_0 (Ref. 54) and P, which arises from fact that P is expected to be inversely proportional to the lattice parameter.[59]

The valence band dispersion near the Γ-point of the Brillouin zone is characterized by the three independent Dresselhaus–Kip–Kittel (DKK) parameters A, B, and $|C|$ (Ref. 55). Expressions for these parameters that account for their temperature dependence have been given in Appendix B of Ref. 60. Because of the strong band warping, hole effective masses can only be defined by appropriate angular averages of the dispersion relations. Since in most expressions the masses appear in quantities involving densities of states, we obtain the heavy- and light-hole masses $m_{hh}^{3/2}$ and $m_{lh}^{3/2}$ as angular averages of the corresponding expressions in terms of A, B, and $|C|$.[60] This gives at 20 °C $m_{hh} = 0.352m_0$ and $m_{lh} = 0.0385m_0$.

For TAT calculations, we need dispersion masses along the [001] direction. These are given by[59]

$$\frac{m_0}{m_{c,hh}} = -A + B \qquad (A6)$$

for heavy holes and by

$$\frac{m_0}{m_{c,lh}} = -A - B \tag{A7}$$

for light holes. We find at $20\,°C$ $m_{c,hh} = 0.403\,m_0$ and $m_{c,lh} = 0.0829\,m_0$. Our semiconductor equations, however, are based on a two-band model that does not distinguish between light and heavy holes, so we compute the hole enhancement function as a weighted average of the heavy- and light-hole enhancement functions,

$$\Gamma_{pt} = \frac{m_{hh}^{3/2}}{m_{hh}^{3/2} + m_{lh}^{3/2}}\Gamma_{hh,t} + \frac{m_{lh}^{3/2}}{m_{hh}^{3/2} + m_{lh}^{3/2}}\Gamma_{lh,t}. \tag{A8}$$

Here, we have chosen weights approximately proportional to the corresponding densities of state. Given the dominance of heavy holes in this respect, the error incurred by making this ad hoc average assumption should be very small.

c. Strain

Ge films grown on Si or other substrates are usually tetragonally distorted due to the lattice mismatch between film and substrate. This mismatch is mostly relaxed in good-quality Ge-on-Si, but the residual levels of strain can still have a non-negligible effect on the I–V characteristics and their temperature dependence, since they affect the bandgaps. We correct for the strain dependence of the bandgaps using the expressions in Ref. 61. We use the same values of the deformation potentials given in this reference except that we take $-b_1 = 2.88\,eV$ and $b_2 = 0\,eV$, consistent with the more recent experimental results of Liu and co-workers.[62] Note that the expressions in Ref. 61 represent an attempt to compute the shifts of individual bands relative to an absolute energy reference, whereas here we are interested in the bandgap strain dependence. This leads to a simplification of the corresponding expressions.

The strain determined experimentally is only valid at the temperature it was measured. For simulations of the temperature dependence of the I–V curves, we need to consider the possibility of additional strain due to the thermal expansivity mismatch between Ge and the substrate or buffer layer used. For Ge-on-Si, this additional strain can be computed based on Eqs. (A1) and (A2) by assuming that the film is forced to track the substrate's thermal expansion.

Strain also affects the effective masses, but we do not include such effects here. Similarly, the weights in the average computed in Eq. (A8) should depend on strain because strain splits the light- and heavy-hole bands, but we also neglect this effect.

d. Bimolecular recombination

Bimolecular recombination plays a very limited role in all diodes examined here, but we included it for completeness. We computed the coefficient B_{bim} using the theory for direct and indirect absorption discussed in Ref. 19. The results for Ge at $20\,°C$ are $B_{bim,dir}/n_i^2 = 8.89 \times 10^{12}\,cm^{-3}\,s^{-1}$ for the direct gap and $B_{bim,ind}/n_i^2 = 1.23 \times 10^{12}\,cm^{-3}\,s^{-1}$ for the fundamental indirect gap.

3. Thermal, transport, and electrical properties

a. Thermal properties

Accurate values of the intrinsic carrier concentration n_i and associated Fermi levels are important for matching theoretical and experimental I–V curves and modeling their temperature dependence. As noted in Ref. 63, there are non-negligible deviations between experimental and theoretical values of n_i if one uses elementary textbook expressions based on the effective masses introduced above. This is due to significant non-parabolicity effects in Ge. Thus, we compute the intrinsic carrier concentrations using the model described in detail in Ref. 19 by setting $n = p$ and solving for the common Fermi level. For these calculations, we use strain-corrected values for the bandgaps included. The only additional deformation potentials needed beyond those described in Ref. 61 are the ones corresponding to the third conduction band minimum along the Δ-direction (which in Si is the absolute conduction band minimum). These deformation potentials are defined in the Appendix of Ref. 64, where recommended values for Si and Ge are given.

b. Mobilities

For the electron mobilities, we use the expressions proposed in Ref. 47 which were fit to experimental data as described there. For the hole mobilities, we use

$$\mu_p = \frac{\mu_{p0}(T)}{1 + \left(\frac{p}{A \times 10^{17}\,cm^{-3}}\right)^{\alpha_0}}, \tag{A9}$$

which we fit to the experimental data from Trumbore and Tartaglia[65] using $\mu_{p0}(T) = 1.05 \times 10^9 \times T^{-2.33}\,cm^2/V\,s$ from Ref. 66. The fit parameters are $A = 1.9349$ and $\alpha_0 = 0.4302$.

c. Recombination lifetimes

Bulk lifetimes The parameters that appear in Eq. (42) must be fit to experimental data. We have attempted to fit results from several references.[67–72] while there is no fully satisfactory fit of the experimental data with a simple analytical expression, we find reasonable agreement assuming a midgap defect and

$$\tau_n = \frac{\tau_{n0}}{1 + N/N_0}\left(\frac{300\,K}{T}\right)^{3/2} \tag{A10}$$

and

$$\tau_n = \frac{\tau_{p0}}{1 + N/N_0}\left(\frac{300\,K}{T}\right)^{3/2}, \tag{A11}$$

with $\tau_{n0} = 5\,\mu s$, $\tau_{p0} = 100\,\mu s$, $N_0 = 8 \times 10^{15}\,cm^{-3}$, and N the dopant density. The temperature dependence is from Schenk.[73]

Dislocation lifetimes Yamaguchi and co-workers derived an expression for the recombination lifetime associated with dislocations that was useful to understand the behavior of GaAs solar cells on Si.[74] However, we find that for the case of Ge-on-Si the

TABLE I. Coefficients of Eq. (23) for each of the independent functions v, u_n, and u_p. Notice that we have introduced a term g'_j not defined in the main text. This term must be added when the diode is illuminated. Explicit expressions for g'_j will be given elsewhere.

	v	u_n	u_p
α_{j+1}	$-\dfrac{2\epsilon'_{j+\frac{1}{2}}}{(h'_j + h'_{j-1})h'_j}$	$\dfrac{2D'_{n,j+\frac{1}{2}}}{(h'_j + h'_{j-1})h'_j} B(v_j - v_{j+1})\exp(v_j)$	$-\dfrac{2D'_{p,j+\frac{1}{2}}}{(h'_j + h'_{j-1})h'_j} B(v_{j+1} - v_j)\exp(-v_j)$
α_{j-1}	$-\dfrac{2\epsilon'_{j-\frac{1}{2}}}{(h'_j + h'_{j-1})h'_{j-1}}$	$\dfrac{2D'_{n,j-\frac{1}{2}}}{(h'_j + h'_{j-1})h'_{j-1}} B(v_j - v_{j-1})\exp(v_j)$	$-\dfrac{2D'_{p,j-\frac{1}{2}}}{(h'_j + h'_{j-1})h'_{j-1}} B(v_{j-1} - v_j)\exp(-v_j)$
α_j	$\alpha_{j+1} + \alpha_{j-1}$	$\alpha_{j+1} + \alpha_{j-1}$	$\alpha_{j+1} + \alpha_{j-1}$
G_j	$\dfrac{n_i}{\bar{N}}\{u_{pj}\exp(-v_j) - u_{nj}\exp(v_j)\}$	$u_{nj}u_{p,j}(r'_j + B'_{j,\text{bim}})$	$-u_{nj}u_{p,j}(r'_j + B'_{j,\text{bim}})$
f_j	$\dfrac{(N_{dj} - N_{aj})}{\bar{N}}$	$-(r'_j + B'_{j,\text{bim}}) - g'_j$	$(r'_j + B'_{j,\text{bim}}) + g'_j$

Yamaguchi expression gives lifetimes that appear too short compared to experimental data. For example, for dislocation densities in the neighborhood of 10^7 cm^{-2}, the expression predicts lifetimes near 100 ps, but the experimental values are in the μs range.[14] Unfortunately, the experimental data are scarce and large variations of more than one order of magnitude are observed for nominally similar dislocation concentrations, suggesting that the correlation between the number of recombination centers and the dislocation density may depend on the precise way dislocations are generated or annealed out. For this reason, attempts to fit general expressions to subsets of the available data seem of dubious general validity. We then take the opposite approach. We start with all existing information, nicely summarized by Son and co-workers,[14] and we add data from DiLello and co-workers.[11] When all these data are combined, a linear dependence between inverse recombination lifetimes and dislocation density cannot be ruled out, although some individual sets of data, such as the results from Eneman and co-workers,[75] are strongly superlinear. We then take the simplest approach and carry out a linear fit, the result being Eq. (51). It is important to point out that our models make it very difficult to distinguish between recombination/generation due to dislocations and contamination during growth. The fact that we fit dislocation densities similar to the measured values suggests that contamination effects are modest.

APPENDIX B: SEMICONDUCTOR EQUATION COEFFICIENTS

We showed above that the discretized semiconductor equations can be all written as shown in Eq. (23). We then defined dimensionless quantities in Eqs. (30)–(33) to facilitate the numerical computations. Table I shows the coefficients of Eq. (23) in terms of those dimensionless quantities.

REFERENCES

[1]M. T. Currie, S. B. Samavedam, T. A. Langdo, C. W. Leitz, and E. A. Fitzgerald, Appl. Phys. Lett. **72**, 1718–1721 (1998).

[2]V. Sorianello, L. Colace, N. Armani, F. Rossi, C. Ferrari, L. Lazzarini, and G. Assanto, Opt. Mater. Express **1**(5), 856–865 (2011).

[3]K. H. Lee, S. Bao, Y. Lin, W. Li, P. Anantha, L. Zhang, Y. Wang, J. Michel, E. A. Fitzgerald, and C. S. Tan, J. Mater. Res. **32**(21), 4025–4040 (2017).

[4]L. Colace and G. Assanto, IEEE Photonics J. **1**(2), 69 (2009).

[5]J. Michel, J. Liu, and L. C. Kimerling, Nat. Photonics **4**(8), 527–534 (2010).

[6]J. Wang and S. Lee, Sensors (Basel) **11**(1), 696–718 (2011).

[7]X. Zhao, M. Moeen, M. S. Toprak, G. Wang, J. Luo, X. Ke, Z. Li, D. Liu, W. Wang, C. Zhao, and H. H. Radamson, J. Mater. Sci.: Mater. Electron. **31**(1), 18–25 (2019).

[8]R. A. Soref, J. Kouvetakis, J. Menéndez, J. Tolle, and V. R. D'Costa, J. Mater. Res. **22**(12), 3281–3291 (2007).

[9]C. L. Senaratne, J. D. Gallagher, T. Aoki, J. Kouvetakis, and J. Menéndez, Chem. Mater. **26**(20), 6033–6041 (2014).

[10]S. Wirths, D. Buca, and S. Mantl, Prog. Cryst. Growth Charact. Mater. **62**(1), 1–39 (2016).

[11]N. A. DiLello, D. K. Johnstone, and J. L. Hoyt, J. Appl. Phys. **112**(5), 054506 (2012).

[12]H. Chen, P. Verheyen, P. De Heyn, G. Lepage, J. De Coster, S. Balakrishnan, P. Absil, G. Roelkens, and J. Van Campenhout, J. Appl. Phys. **119**(21), 213105 (2016).

[13]E. Simoen, B. Hsu, G. Eneman, E. Rosseel, R. Loo, H. Arimura, N. Horiguchi, W. C. Wen, H. Nakashima, C. Claeys, A. Oliveira, P. Agopian, and J. Martino, paper presented at the 2019 34th Symposium on Microelectronics Technology and Devices (SBMicro) (2019).

[14]B. Son, Y. Lin, K. H. Lee, Q. Chen, and C. S. Tan, J. Appl. Phys. **127**(20), 203105 (2020).

[15]A. Pizzone, S. A. Srinivasan, P. Verheyen, G. Lepage, S. Balakrishnan, and J. V. Campenhout, paper presented at the 2020 IEEE Photonics Conference (IPC) (2020).

[16]X. Zhao, G. Wang, H. Lin, Y. Du, X. Luo, Z. Kong, J. Su, J. Li, W. Xiong, Y. Miao, H. Li, G. Guo, and H. H. Radamson, Nanomaterials (Basel) **11**(5), 1125 (2021).

[17]C. Xu, R. T. Beeler, L. Jiang, G. Grzybowski, A. V. G. Chizmeshya, J. Menéndez, and J. Kouvetakis, Semicond. Sci. Technol. **28**(10), 105001 (2013).

[18]S. M. Sze, *Physics of Semiconductor Devices* (Wiley, New York, 1981).

[19]J. Menéndez, C. D. Poweleit, and S. E. Tilton, Phys. Rev. B **101**(19), 195204 (2020).

[20]E. Rosencher and B. Vinter, *Optoelectronics* (Cambridge University, Cambridge, 2002).

[21]C. E. Korman and I. D. Mayergoyz, J. Appl. Phys. **68**(3), 1324–1334 (1990).

[22]D. L. Scharfetter and H. K. Gummel, IEEE Trans. Electron Devices **16**(1), 64–77 (1969).

[23]C. M. Snowden, *Semiconductor Device Modelling* (Peter Peregrinus, 1988).

06 April 2024 06:05:22

[24]H. Sundqvist and G. Veronis, Tellus A **22**(1), 26 (1970).

[25]I. D. Mayergoyz, J. Appl. Phys. **59**(1), 195–199 (1986).

[26]W. W. Keller, J. Appl. Phys. **61**(11), 5189–5190 (1987).

[27]T. I. Seidman and S. C. Choo, Solid-State Electron. **15**(11), 1229–1235 (1972).

[28]W. H. Press, S. A. Teukolsky, W. T. Vetterling, and B. P, in *Flannery, Numerical Recipes in C: The Art of Scientific Computing*, 2nd ed. (Cambridge University, New York, 1992).

[29]G. A. M. Hurkx, D. B. M. Klaassen, and M. P. G. Knuvers, IEEE Trans. Electron Devices **39**(2), 331–338 (1992).

[30]R. N. Sajjad, W. Chern, J. L. Hoyt, and D. A. Antoniadis, "Trap assisted tunneling and its effect on subthreshold swing of tunnel FETs," IEEE Transactions on Electron Devices **63**, 4380–4387 (2016).

[31]W. Takeuchi, T. Asano, Y. Inuzuka, M. Sakashita, O. Nakatsuka, and S. Zaima, ECS J. Solid State Sci. Technol. **5**(4), P3082–P3086 (2015).

[32]S. Gupta, E. Simoen, R. Loo, Y. Shimura, C. Porret, F. Gencarelli, K. Paredis, H. Bender, J. Lauwaert, H. Vrielinck, and M. Heyns, Appl. Phys. Lett. **113**(2), 022102 (2018).

[33]B. Wang, Z. Q. Fang, B. Claflin, D. Look, J. Kouvetakis, and Y. K. Yeo, Thin Solid Films **654**, 77–84 (2018).

[34]A. Czerwinski, E. Simoen, A. Poyai, and C. Claeys, J. Appl. Phys. **94**(2), 1218–1221 (2003).

[35]L. Colace, G. Masini, F. Galluzzi, G. Assanto, G. Capellini, L. D. Gaspare, E. Palange, and F. Evangelisti, Appl. Phys. Lett. **72**(24), 3175–3177 (1998).

[36]L. Colace, P. Ferrara, G. Assanto, D. Fulgoni, and L. Nash, IEEE Photonics Technol. Lett. **19**(22), 1813 (2007).

[37]M. Balbi, V. Sorianello, L. Colace, and G. Assanto, Physica E **41**(6), 1086–1089 (2009).

[38]Y.-Y. Fang, J. Tolle, J. Tice, A. V. G. Chizmeshya, J. Kouvetakis, V. R. D'Costa, and J. Menéndez, Chem. Mater. **19**(24), 5910–5925 (2007).

[39]G. Grzybowski, L. Jiang, R. T. Beeler, T. Watkins, A. V. G. Chizmeshya, C. Xu, J. Menéndez, and J. Kouvetakis, Chem. Mater. **24**(9), 1619–1628 (2012).

[40]G. Grzybowski, A. V. G. Chizmeshya, C. Senaratne, J. Menendez, and J. Kouvetakis, J. Mater. Chem. C **1**(34), 5223 (2013).

[41]C. Xu, J. D. Gallagher, P. M. Wallace, C. L. Senaratne, P. Sims, J. Menéndez, and J. Kouvetakis, Semicond. Sci. Technol. **30**(10), 105028 (2015).

[42]A. Zhang, M. A. Mircovich, D. A. Ringwala, C. D. Poweleit, M. A. Roldan, J. Menéndez, and J. Kouvetakis, J. Mater. Chem. C **10**(36), 13107–13116 (2022).

[43]C. Xu, C. L. Senaratne, J. Kouvetakis, and J. Menéndez, Appl. Phys. Lett. **105**(23), 232103 (2014).

[44]C. Xu, C. L. Senaratne, J. Kouvetakis, and J. Menéndez, Phys. Rev. B **93**(4), 041201 (2016).

[45]C. Xu, N. S. Fernando, S. Zollner, J. Kouvetakis, and J. Menéndez, Phys. Rev. Lett. **118**(26), 267402 (2017).

[46]C. Xu, J. Kouvetakis, and J. Menéndez, J. Appl. Phys. **125**(8), 085704 (2019).

[47]J. Menéndez, C. Xu, and J. Kouvetakis, Mater. Sci. Semicond. Process. **164**, 107596 (2023).

[48]C. Xu, T. Hu, D. A. Ringwala, J. Menéndez, and J. Kouvetakis, J. Vac. Sci. Technol., A **39**(6), 063411 (2021).

[49]V. R. D'Costa, Y. Fang, J. Mathews, R. Roucka, J. Tolle, J. Menéndez, and J. Kouvetakis, Semicond. Sci. Technol. **24**(11), 115006 (2009).

[50]C. Xu, P. M. Wallace, D. A. Ringwala, J. Menéndez, and J. Kouvetakis, ACS Appl. Mater. Interfaces **10**(43), 37198–37206 (2018).

[51]R. Roucka, Y. Y. Fang, J. Kouvetakis, A. V. G. Chizmeshya, and J. Menéndez, Phys. Rev. B **81**(24), 245214 (2010).

[52]H. Ibach, Phys. Status Solidi B **33**(1), 257–265 (1969).

[53]Y. Ma and J. S. Tse, Solid State Commun. **143**(3), 161 (2007).

[54]C. Emminger, N. S. Samarasingha, M. Rivero Arias, F. Abadizaman, J. Menéndez, and S. Zollner, J. Appl. Phys. **131**(16), 165701 (2022).

[55]G. Dresselhaus, A. Kip, and C. Kittel, Phys. Rev. **98**(2), 368–384 (1955).

[56]D. Rideau, M. Feraille, L. Ciampolini, M. Minondo, C. Tavernier, H. Jaouen, and A. Ghetti, Phys. Rev. B **74**(19), 195208 (2006).

[57]R. L. Aggarwal, Phys. Rev. B **2**(2), 446–458 (1970).

[58]D. E. Aspnes, Phys. Rev. B **12**(6), 2297–2310 (1975).

[59]P. Y. Yu and M. Cardona, *Fundamentals of Semiconductors: Physics and Materials Properties* (Springer-Verlag, Berlin, 1996).

[60]J. Menéndez, D. J. Lockwood, J. C. Zwinkels, and M. Noël, Phys. Rev. B **98**(16), 165207 (2018).

[61]J. Menendez and J. Kouvetakis, Appl. Phys. Lett. **85**(7), 1175–1177 (2004).

[62]J. Liu, D. D. Cannon, K. Wada, Y. Ishikawa, D. T. Danielson, S. Jongthammanurak, J. Michel, and L. Kimerling, Phys. Rev. B **70**(15), 155309 (2004).

[63]J. Menéndez, P. M. Wallace, C. Xu, C. L. Senaratne, J. D. Gallagher, and J. Kouvetakis, Mater. Today: Proc. **14**, 38–42 (2019).

[64]J. Teherani, W. Chern, D. Antoniadis, J. Hoyt, L. Ruiz, C. Poweleit, and J. Menéndez, Phys. Rev. B **85**(20), 205308 (2012).

[65]F. A. Trumbore and A. A. Tartaglia, J. Appl. Phys. **29**(10), 1511 (1958).

[66]O. Madelung, in *Landolt-Börstein: Numerical Data and Functional Relationships in Science and Technology*, edited by K. H. Hellwege (Springer-Verlag, Berlin, 1985), Vol. 17A.

[67]E. Gaubas, M. Bauža, A. Uleckas, and J. Vanhellemont, Mater. Sci. Semicond. Process. **9**(4–5), 781–787 (2006).

[68]E. Gaubas and J. Vanhellemont, Appl. Phys. Lett. **89**(14), 142106 (2006).

[69]E. Gaubas and J. Vanhellemont, J. Electrochem. Soc. **154**(3), H231 (2007).

[70]E. Gaubas, J. Vanhellemont, E. Simoen, I. Romandic, W. Geens, and P. Clauws, Phys. B: Condens. Matter. **401–402**, 222–225 (2007).

[71]B. P. Swain, H. Takato, Z. Liu, and I. Sakata, Sol. Energy Mater. Sol. Cells **95**(1), 84–88 (2011).

[72]B. P. Swain, H. Takato, and I. Sakata, Jpn. J. Appl. Phys. **50**(7), 071302 (2011).

[73]A. Schenk, Solid-State Electron. **35**(11), 1585–1596 (1992).

[74]M. Yamaguchi, A. Yamamoto, and Y. Itoh, J. Appl. Phys. **59**(5), 1751–1753 (1986).

[75]G. Eneman, M. Bargallo Gonzalez, G. Hellings, B. De Jaeger, G. Wang, J. Mitard, K. DeMeyer, C. Claeys, M. Meuris, M. Heyns, T. Hoffmann, and E. Simoen, ECS Trans. **28**(5), 143 (2010).

06 April 2024 06:05:22